

METAL-POOR, COOL GAS IN THE CIRCUMGALACTIC MEDIUM OF A $Z = 2.4$ STAR-FORMING GALAXY: DIRECT EVIDENCE FOR COLD ACCRETION?*

NEIL H. M. CRIGHTON¹, JOSEPH F. HENNAWI¹ & J. XAVIER PROCHASKA^{1,2}

Draft version August 23, 2013

ABSTRACT

In our current galaxy formation paradigm, high-redshift galaxies are predominantly fuelled by accretion of cool, metal-poor gas from the intergalactic medium. Hydrodynamical simulations predict that this material should be observable in absorption against background sightlines within a galaxy’s virial radius, as optically thick Lyman-limit systems (LLSs) with low metallicities. Here we report the discovery of exactly such a strong metal-poor absorber at an impact parameter $R_{\perp} = 58$ kpc from a star-forming galaxy at $z = 2.44$. Besides strong neutral hydrogen ($N_{\text{H}^0} = 10^{19.50 \pm 0.16} \text{ cm}^{-2}$) we detect neutral deuterium and oxygen, allowing a precise measurement of the metallicity: $\log_{10}(Z/Z_{\odot}) = -2.0 \pm 0.17$, or $(7 - 15) \times 10^{-3}$ solar. Furthermore, the narrow deuterium linewidth requires a cool temperature $< 20,000$ K. Given the striking similarities between this system and the predictions of simulations, we argue that it represents the direct detection of a high redshift cold-accretion stream. The low-metallicity gas cloud is a single component of an absorption system exhibiting a complex velocity, ionization, and enrichment structure. Two other components have metallicities > 0.1 solar, ten times larger than the metal-poor component. We conclude that the photoionized circumgalactic medium (CGM) of this galaxy is highly inhomogeneous: the majority of the gas is in a cool, metal-poor and predominantly neutral phase, but the majority of the metals are in a highly-ionized phase exhibiting weak neutral hydrogen absorption but strong metal absorption. If such inhomogeneity is common, then high-resolution spectra and detailed ionization modelling are critical to accurately appraise the distribution of metals in the high-redshift CGM.

Subject headings: galaxies: halos — galaxies: evolution — galaxies: high-redshift — quasars: absorption lines — intergalactic medium

1. INTRODUCTION

It is now recognized that the physical processes by which galaxies accrete, expel and recycle baryons are of central importance to galaxy evolution (e.g. Davé et al. 2012). The current theoretical paradigm emphasizes a ‘cold-mode’ of accretion (Birnboim & Dekel 2003; Kereš et al. 2005) that fuels the high star formation rates (SFRs) observed in the early universe. This cool ($T \sim 10^4$ K), accreting gas is predicted to produce observable signatures as high column density, low metallicity absorption systems (Fumagalli et al. 2011; Faucher-Giguère & Kereš 2011; Stewart et al. 2011; van de Voort et al. 2012; Kimm et al. 2011; Goerdts et al. 2012; Nelson et al. 2013) in the spectra of background sightlines which pass through the circumgalactic medium (CGM) of high redshift galaxies. However, there is little direct observational evidence for the cold-accretion phenomenon. Instead, metal-enriched outflows are commonly observed from $z \sim 2 - 3$ Lyman-break galaxies (LBGs) as blue-shifted absorption features in the galaxies’ spectra (Pettini et al. 2001; Steidel et al. 2010). Energetic ‘feedback’ in some form is required to regulate star formation in numerical simulations, which is necessary to match observables such as the stellar luminosity function

(Oppenheimer et al. 2010) and galaxy rotation curves (Stinson et al. 2013), but the distances to which these outflows travel and their energetics are poorly constrained. Precise measurements of the enrichment and physical conditions of the CGM are thus crucial both to test the cold accretion picture and to characterize how far outflowing material travels.

The best technique currently available to measure metallicities is by analyzing individual absorption line profiles from gas in the CGM. This technique has been used extensively to measure metallicities of high column density systems over a broad redshift range (e.g. Steidel 1990; Lehner et al. 2013). However, the relationship between the absorbing gas and galaxies in these studies is often unclear, making them difficult to interpret in the context of galaxy formation models. The cold accretion phenomenon may persist to lower redshifts in lower mass haloes, and several observational studies have discovered low metallicity ($Z/Z_{\odot} = 0.01 - 0.1$) absorbers in the neighbourhood of $z < 1$ galaxies (e.g. Chen et al. 2005; Tripp et al. 2005; Ribaldo et al. 2011; Kacprzak et al. 2012; Churchill et al. 2012). But measurements of CGM enrichment near vigorously star-forming galaxies at $z \sim 2.5$, during the peak of the cosmic SFR and where cold accretion is predicted to occur over a wide range of halo masses, have proven to be much more challenging.

In this letter we analyze an echelle spectrum of a background QSO at an impact parameter of 58 kpc from a foreground star-forming galaxy discovered by

* Data and code used for this paper are available at <http://github.com/nhmc/z2.4CGM>

¹ Max-Planck-Institut für Astronomie, Königstuhl

² Department of Astronomy and Astrophysics, UCO/Lick Observatory; University of California, 1156 High Street, Santa Cruz, CA 95064; xavier@ucolick.org

Rudie et al. (2012)⁴. The high signal-to-noise ratio ($S/N \sim 90$), high-resolution ($\text{FWHM} \sim 8.8 \text{ km s}^{-1}$) spectrum combined with the rare detection of the deuterium isotope of hydrogen, enable us to effectively disentangle absorption produced by neutral, metal poor gas from that of more highly ionized, metal enriched gas. The deuterium detection allows us to precisely measure the metallicity of a metal-poor CGM absorber, and we show that it exhibits many of the characteristics expected for cold-mode accretion.

2. OBSERVATIONS AND ANALYSIS

2.1. The Background QSO and Foreground Galaxy

The bright background QSO J1444535+291905 ($g = 16.4$) at redshift $z = 2.660$ has been observed using the HIRES echelle spectrograph on Keck by several groups from 1995 to 2009. We obtained the spectra from the Keck archive and reduced them with MAKEE⁵. The final combined spectrum covers wavelength ranges 3100 to 5950 Å (resolution 8.8 km s^{-1}) and 7350 to 9760 Å (resolution 6.7 km s^{-1}).

The foreground galaxy's redshift ($z_{gal} = 2.4391$) and impact parameter from the background QSO ($R_{\perp} = 58 \text{ kpc}$) are given by Rudie et al. (2012, their figure 12). The redshift uncertainty is $160 - 180 \text{ km s}^{-1}$, which arises when rest-frame UV transitions such as Ly α emission and metal absorption are used to determine the intrinsic redshift (Rakic et al. 2011). Rudie et al. do not publish further details on the galaxy, but such galaxies typically have a dust-extinction corrected SFR of $30 M_{\odot} \text{ yr}^{-1}$ (Erb et al. 2006b), a gas-phase ISM metallicity of $Z/Z_{\odot} \sim 0.8$ (Erb et al. 2006a) and a dark matter halo mass $5 \times 10^{11} M_{\odot}$ (Bielby et al. 2013). This halo mass implies a virial radius of 75 kpc (Bryan & Norman 1998), and thus the projected separation from the background QSO sightline is comparable to the virial radius.

We note that Rudie (2013) indicates a second star-forming galaxy is present at $R_{\perp} = 50 \text{ kpc}$ within 250 km s^{-1} of the first galaxy, but does not publish the spectroscopic redshift. We adopt $R_{\perp} = 58 \text{ kpc}$ for our analysis, but our conclusions remain unchanged if a second galaxy exists at an even closer impact parameter.

2.2. The Absorption System at $z = 2.44$

The HIRES spectrum reveals a sub-damped absorption system, originally discovered by (Simcoe et al. 2002), that is coincident with the redshift of the foreground galaxy. Our Voigt profile fit to the damping wings implies a total neutral hydrogen column density $N_{\text{H}^0} = 10^{19.85 \pm 0.1} \text{ cm}^{-2}$ (Figure 1, top). Absorption from low and high-ionization ionic metal line transitions is present in 16 distinct components spread across 320 km s^{-1} (Figure 2). The total N_{H^0} is well-constrained, but as we will demonstrate, the metallicity varies by an order of magnitude among the components. Fortunately, we can also constrain N_{H^0} for several *individual* components.

We measured column densities in the system by fitting Voigt profiles with VPFIT⁶, and by using the apparent

optical depth (AOD, Savage & Sembach 1991) method. Voigt profile fits assess the degree to which a single kinematic model can explain all the observed absorption: low-ionization transitions were used to define the main velocity components, and we found that a single velocity structure matches all the low-ionization species well. The resulting models are shown in Figures 1 & 2. The higher ionization transitions Si IV, C IV and O VI do not follow the same velocity structure as the low-ions, indicating there is likely a contribution from a hotter or more highly-ionized phase. Similar offsets between low and high-ions have been observed in other high- z absorbers (e.g. Fox et al. 2007). Table 1 gives Voigt profile parameters and our adopted column densities for each component. Our Voigt profile fits to both the high-ions and low-ions show no evidence for partial covering or unresolved saturated components.

2.3. Components for which Abundances Can be Precisely Measured

We identify three kinematic regions for which the neutral hydrogen column N_{H^0} , and thus the metallicity, can be precisely measured. The first is at -218 km s^{-1} relative to the galaxy redshift, where absorption from neutral deuterium is detected at Ly- γ , Ly- δ , Ly- ϵ and Ly-8. Deuterium detections in QSO absorbers are rare, as a measurement of the weak D absorption requires a narrow linewidth, high N_{H^0} , and the absence of blending with weaker neighbouring Ly α forest lines (Webb et al. 1991). Such detections are valuable however, because a precise D/H measurement constrains the cosmic baryon density according to big bang nucleosynthesis theory. For the D component we detect, $N_{\text{D}^0} = 10^{14.93 \pm 0.06} \text{ cm}^{-2}$ and $b(\text{D}^0) = 10.60 \pm 0.53 \text{ km s}^{-1}$, which are consistent with the expected column density and width of the associated H^0 , estimated from the damping wings and the Lyman series, assuming thermal broadening and the cosmic D/H ratio inferred from the WMAP cosmic baryon density (Keisler et al. 2011). This width is much narrower than is typical for a Ly α forest line with the $N_{\text{H}^0} \approx 10^{15} \text{ cm}^{-2}$ necessary to imitate D I, which demonstrates that this is not an interloping Ly α forest line.

We can use the D/H ratio implied by the cosmic baryon density to make a precise measurement of N_{H^0} in this component. Pettini & Cooke (2012) find $\log_{10}(\text{D}/\text{H}) = -4.585 \pm 0.02$ in QSO absorbers. The standard deviation in these QSO values (0.15) is larger than that expected from the measurement errors, and represents real scatter due to an unidentified astrophysical effect and/or underestimated systematic errors in the D/H analyses. We conservatively assume the scatter represents a physical variation and take $\log_{10}(\text{D}/\text{H}) = -4.585 \pm 0.15$. D^0/H^0 is the same as D/H, and therefore $\log_{10} N_{\text{H}^0} = 19.50 \pm 0.16$ for this component.

Crucially, we also detect O I in this component, which allows a direct measurement of the metallicity from O^0/H^0 . For $N_{\text{H}^0} \gtrsim 10^{19} \text{ cm}^{-2}$, the ion ratio O^0/H^0 is a robust metallicity indicator, because the ionization potentials of O^0 and H^0 are very similar and the two species exchange electrons (Field & Steigman 1971), and O does not deplete strongly onto dust grains (Jenkins 2009). We find $[\text{O}/\text{H}] = -2.00 \pm 0.17$, which is comparable to the background metallicity of the IGM at this

⁴ All distances given are proper, assuming $H_0 = 70 \text{ km s}^{-1} \text{ Mpc}^{-1}$, $\Omega_M = 0.3$ and $\Omega_{\Lambda} = 0.7$.

⁵ <http://www.astro.caltech.edu/~tb/makee/>

⁶ <http://www.ast.cam.ac.uk/~rfc/vpfit.html>

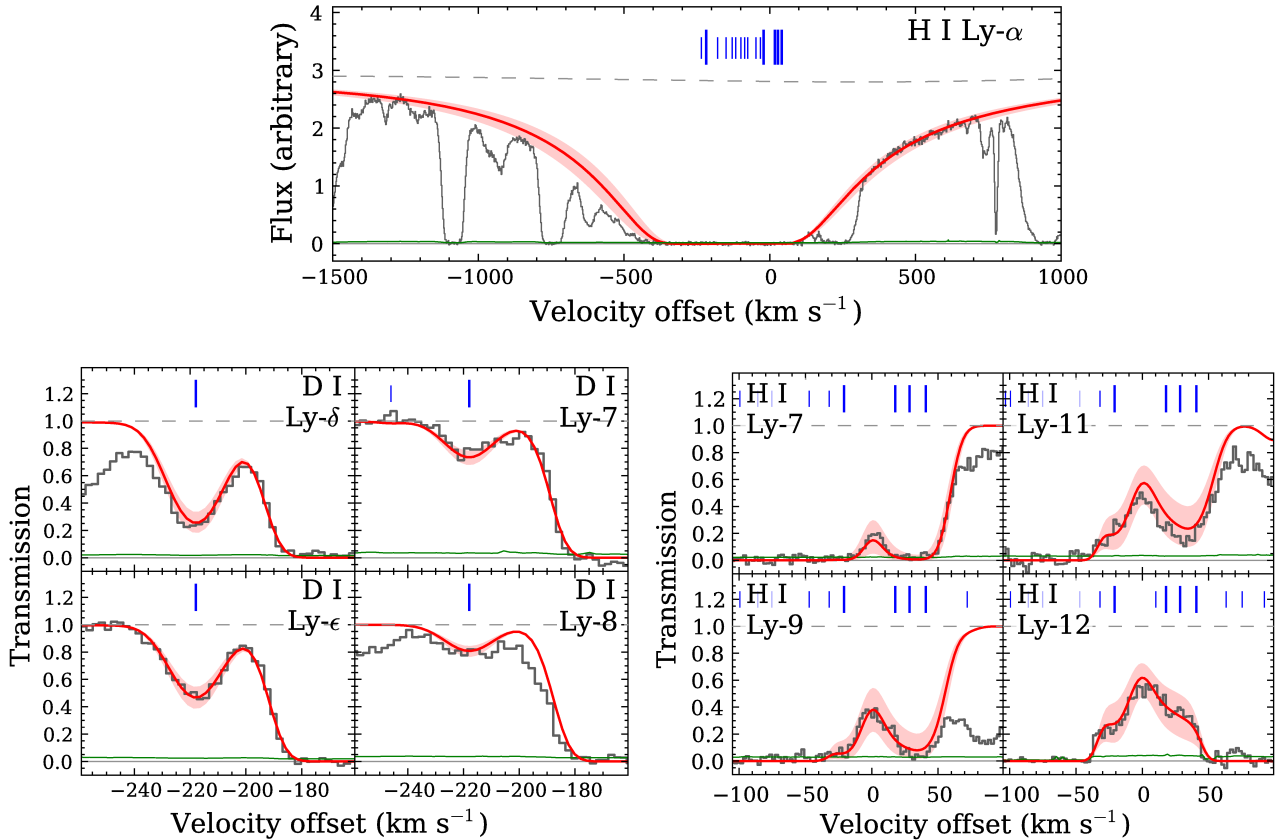


Figure 1. HIRES spectra showing absorption from the D and partial LLS components, marked with long ticks. Shorter ticks show other low-ionization metal components without tight constraints on N_{H^0} . Velocities are relative to $z = 2.4391$, and our best-fitting model is plotted over the data. Panels show H I Ly α (top), and deuterium absorption from the D component (left) and H I for the partial LLS components (right). Shaded regions around the model show the effect of our adopted column density uncertainties for H^0 and D^0 .

redshift (Schaye et al. 2003; Simcoe et al. 2004).

The remaining components for which we can accurately measure N_{H^0} are partial Lyman limit systems at ~ -20 and $\sim +30$ km s^{-1} (Partial LLS 1 & 2, see Figure 2). These show unsaturated H I absorption at the Ly-10, Ly-11 and Ly-12 transitions, which imply $N_{\text{H}^0} = 10^{16.30 \pm 0.20}$ (Partial LLS 1) and $10^{16.43 \pm 0.30} \text{ cm}^{-2}$ (Partial LLS 2). Since ionization corrections are significant at these N_{H^0} , we estimate the metallicity of these components using the photoionization models described in the following section.

2.4. Photoionization Modelling

We use CLOUDY photoionization models (version 8.01 Ferland et al. 1998) to predict the metal ion column densities for the D and partial LLS components given a metallicity and ionization parameter U (defined as the ratio of the densities of ionizing photons to hydrogen atoms). All models assume solar abundance ratios, no dust, and an ionizing spectrum due to the ambient UV background (Haardt & Madau 2012)⁷. We use a maximum likelihood technique to find the best-fitting metallicity and ionization parameter for each component (Crighton et al., in preparation) and their uncertainties. Column densities for low-ions together with upper limits on high-ions are used to constrain the models. Figure 3

⁷ we also consider a spectrum dominated by a starburst galaxy, but it does not significantly affect our results.

shows the models for the D component and partial LLS components, each at the best-fitting metallicity for that component.

For all three components we find that the UV background models provide a good match to the data. For the partial LLS components there is a minor discrepancy for N_{Al^+} , which is 0.3 – 0.4 dex lower than predicted by the models. This could be due to uncertainties in the shape of the ionizing spectrum, although using a starburst-dominated ionizing spectrum makes the disagreement more severe. We believe this discrepancy is likely due to an Al underabundance relative to a solar abundance pattern (e.g. Rolleston et al. 2003). The predicted N^+ column is close to the observed upper limit for Partial LLS 2, which may indicate that nitrogen is underabundant relative to solar. A nitrogen underabundance is often observed in damped systems at a similar redshift (e.g. Prochaska et al. 2002). For all other ionic species there is excellent agreement between the observed column densities and model predictions.

2.5. Physical Conditions in the Absorption System

We have used two independent methods to show that the metallicity of the D component is $\sim 1/100$ solar: $Z/Z_{\odot} = 10^{-2.00 \pm 0.17}$ using O^0/H^0 , and $Z/Z_{\odot} = 10^{-1.92 \pm 0.18}$ from the CLOUDY models using all the metal transitions except O I. The width of the D I line requires a gas temperature $< 20,000$ K, conservatively assuming thermal broadening such that $b = \sqrt{2kT/m_{\text{D}}}$.

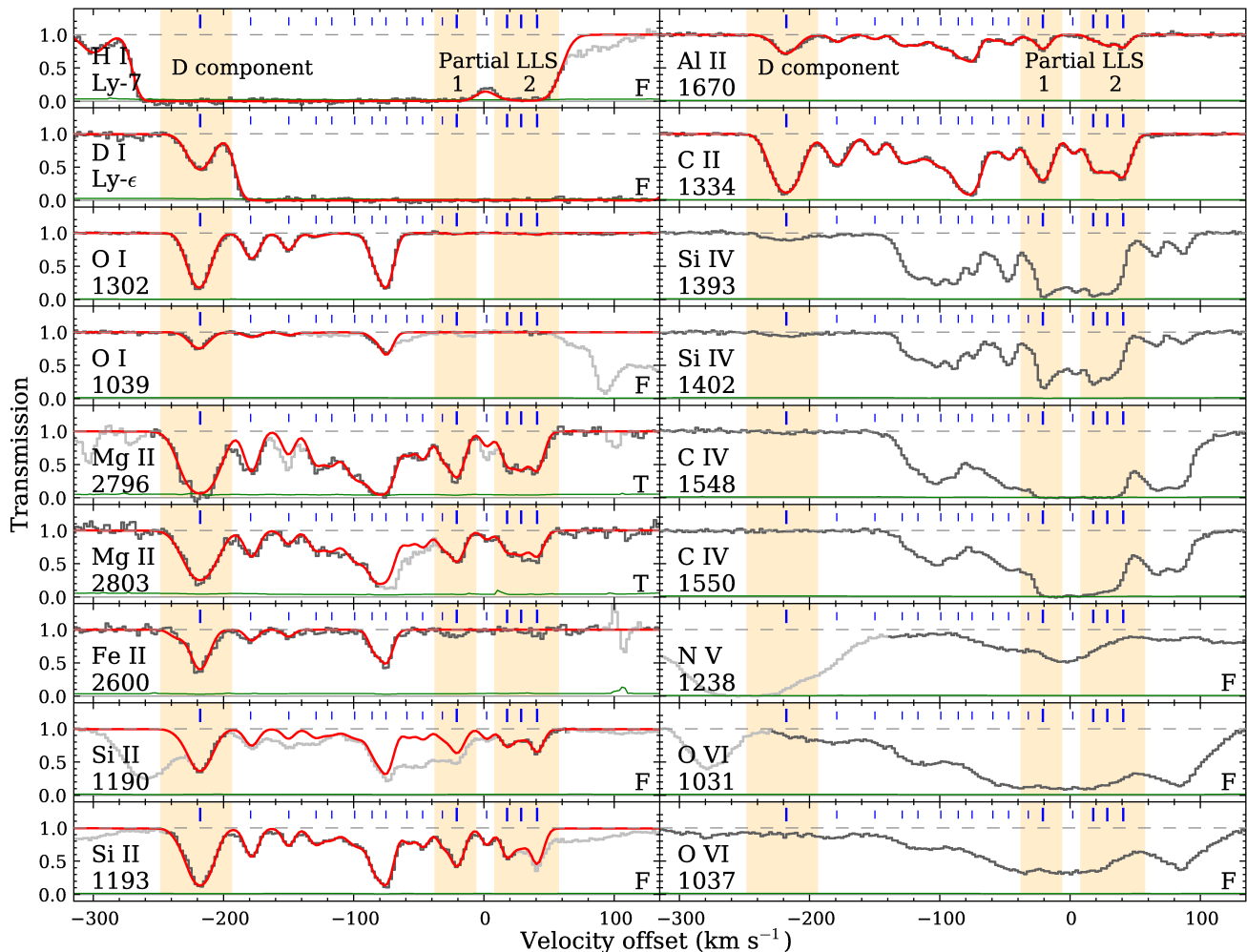


Figure 2. Hires spectra showing metal transitions for the $z = 2.44$ absorption system. Velocities are relative to $z = 2.4391$, and our best-fitting model is plotted over the data. ‘F’ indicates there is blending with Ly α forest absorption; ‘T’ blending with telluric lines. Shading marks regions used to measure AOD column densities, and greyed out lines show regions heavily blended with unrelated forest or telluric absorption.

From the models we find $\log_{10} U = -4.2 \pm 0.95$, which implies that H is $\sim 75\%$ neutral ($N_{\text{H}} \sim 10^{19.6} \text{ cm}^{-2}$) and has a temperature of $\sim 10,000$ K, in agreement with $b(\text{D I})$. $[\text{Fe}/\text{O}] = -0.10 \pm 0.09$, therefore there is no evidence for strong dust depletion, as is expected from the low metallicity. The maximum U permitted ($10^{-3.2}$) corresponds to a neutral fraction of 25% and $n_{\text{H}} = 10^{-1.8} \text{ cm}^{-3} \times F_{\nu}^{912} / (3 \times 10^{-21} \text{ erg s}^{-1} \text{ cm}^{-2} \text{ Hz}^{-1})$, where F_{ν}^{912} is the magnitude of the ionizing spectrum at 912 Å. This implies a cloud thickness $\lesssim 3$ kpc.

In contrast to the D component, Partial LLS 1 and 2 are metal enriched and highly ionized. Both LLS have similar conditions: the models yield $Z/Z_{\odot} = 10^{-0.44 \pm 0.31}$ ($n_{\text{H}} \approx 10^{-2} \text{ cm}^{-3} \times F_{\nu}^{912} / (3 \times 10^{-21} \text{ erg s}^{-1} \text{ cm}^{-2} \text{ Hz}^{-1})$) and $\log_{10} U = -3.10 \pm 0.15$, implying that less than 1% of H is neutral ($N_{\text{H}} \sim 10^{19} \text{ cm}^{-2}$). Using a starburst-dominated ionizing spectrum allows a lower $Z/Z_{\odot} = 10^{-0.8 \pm 0.32}$, but results in a 0.6-0.7 dex disagreement between the observed and predicted $N_{\text{Al}^{+}}$. Therefore we prefer the UVB-only models, but our main conclusions are unchanged if we were to instead use a starburst-dominated spectrum. A further difference between the D and partial LLS components is the presence of absorp-

tion from higher ionization gas (Si IV, C IV, O VI) over the same velocity range as the low-ions. While some Si IV components align with the low-ions, overall the high-ions have a different velocity structure, and are much stronger than expected from our photoionization modelling of the low-ions. Very broad components are also present in O VI (see Figure 2). Thus these high-ions may trace another gas phase that is shock-heated and collisionally ionized (see e.g. Simcoe et al. 2002).

Finally, we calculate $[\text{O}/\text{H}]$ for the entire system, including all low-ion components, assuming O^0 is associated with the bulk of the H^0 and that ionization corrections are negligible. This gives $[\text{O}/\text{H}]_{\text{total}} = -1.89 \pm 0.11$. Therefore all the O I components, spanning $\sim 140 \text{ km s}^{-1}$, must have a metallicity similar to the D component.

3. DISCUSSION

Figure 4 shows the current state of gas-absorption metallicities measured around $z \sim 2.5$ LBGs. Enriched gas with $Z/Z_{\odot} \gtrsim 0.3$ is found in the partial LLS component in this paper at $R_{\perp} = 58$ kpc, for the galaxy-absorber pair at $R_{\perp} = 110$ kpc from Simcoe et al. (2006), and in the ISM of the gravitationally-lensed LBG

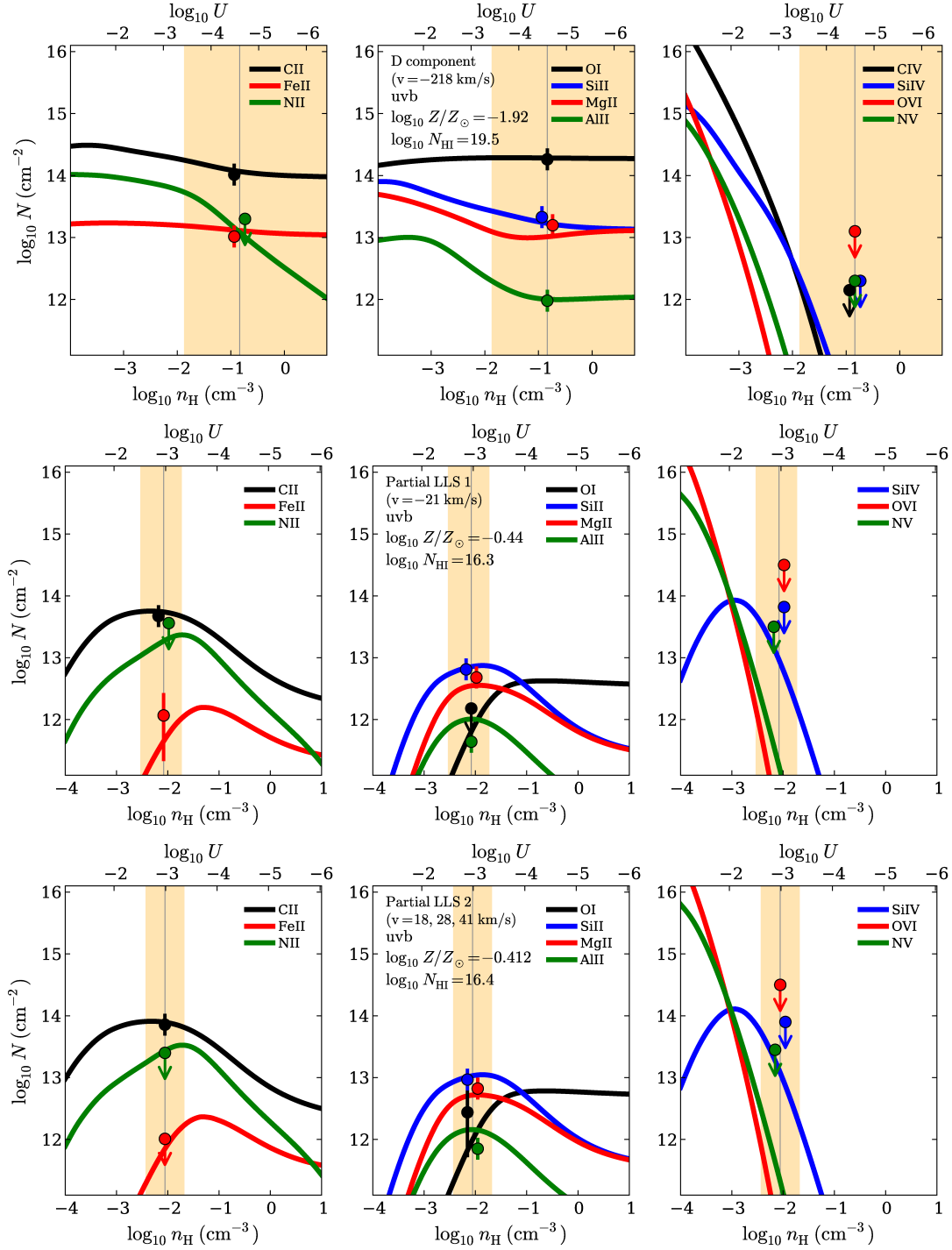


Figure 3. CLOUDY models for the D component (top), Partial LLS 1 (middle) and 2 (bottom). Curves show the model predictions, and points show the observed values and uncertainties at the best-fitting U values, sometimes offset for clarity. The shaded region shows the U range consistent with the data. Error bars include the observed column density uncertainty and a 0.15 dex uncertainty to account for relative abundance variations.

cB58 (Pettini et al. 2002), shown at $R_{\perp} \sim 4$ kpc. Systems at larger separations, also from Simcoe et al., approach the metallicity of the surrounding IGM, suggesting that enriched gas is common in the CGM up to $R_{\perp} \sim 100$ kpc. Also shown are measurements from highly-neutral damped systems with nearby galaxies (Krogager et al. 2012; Bouché et al. 2013). However, we caution that these systems were pre-selected based on

their absorption properties, and so they may not be representative of the typical circumgalactic medium. The metallicity of the D component is more than an order of magnitude lower than the typical ISM metallicity of LBGs (Pettini et al. 2002), indicating that this gas has not been recently stripped or ejected in a wind from the galaxy. Could it be produced by a cold-mode ac-

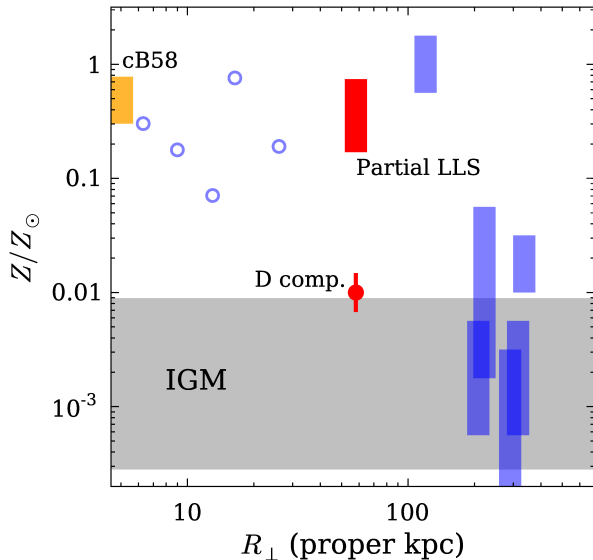


Figure 4. Metallicity of gas associated with $z \sim 2.5$ LBGs as a function of impact parameter. The ISM metallicity measured in the lensed LBG cB58 is shown at $R_{\perp} = 4$ kpc. Other $R_{\perp} < 30$ kpc measurements are for galaxies found by targeted searches around known neutral, damped systems. The D component and partial LLSs are shown by a red circle and red rectangle. Measurements at larger separations are from Simcoe et al. (2006).

cretion flow? It is close to the virial radius⁸, has a high column density ($10^{19.50 \pm 0.16} \text{ cm}^{-2}$), low metallicity ($10^{-2.00 \pm 0.17}$), cool temperature ($20,000 \text{ K} \ll T_{\text{virial}} \approx 10^6 \text{ K}$), and characteristic size $\lesssim 3$ kpc, which are all properties of inflowing streams expected from simulations (e.g. Fumagalli et al. 2011). Stewart et al. (2011) predict that accreting streams have high angular momentum and often co-rotate with the galaxy’s disk, producing offsets of up to 100 km s^{-1} from the systemic galaxy redshift. The D component is at $-218 \pm 180 \text{ km s}^{-1}$ from the nearby galaxy, which is compatible with such an offset. All of the O I components in the absorber, covering a velocity range of $\sim 140 \text{ km s}^{-1}$, also have low metallicities. Such velocity separations are seen by Stewart et al. when a sightline intersects multiple accreting streams. Therefore, in light of all the evidence above, we believe that this absorber represents the best existing candidate for a cold-mode accretion flow at high redshift.

The CGM around this galaxy is highly inhomogeneous: the D and partial LLS components have metallicities that differ by at least a factor of ten. These different metallicities are reminiscent of the bimodal metal distribution seen in $z < 1$ Lyman limit systems (Lehner et al. 2013), which Lehner et al. argue results from physically distinct processes: metal-poor accreting gas, and metal-enriched gas stripped from galaxies or ejected in large-scale winds. Indeed, the two components in this system show further differences besides the metallicity: the D component is neutral and has very weak high-ion absorption, whereas the partial LLSs are highly ionized and have strong associated high-ions. These high-ions are not produced by the same ionizing spectrum that can reproduce the low-ions, and they may be caused by

shock-heated, collisionally-ionized gas that is expected in a supernovae-driven outflowing wind (e.g. Simcoe et al. 2006). This is also consistent with the hydrodynamical simulations of Shen et al. (2013), which indicate that enriched outflowing and metal-poor inflowing phases of the CGM are mixed kinematically.

If such a bimodality is common, as is implied by analyses of other $z \sim 3$ sub-DLAs (e.g. Prochter et al. 2010), it has fundamental implications for interpreting observations of the CGM. Using the N_{H} values inferred from photoionization modelling and the component metallicities, we conclude that the highly ionized partial LLSs contain *most* of the total metal mass in this system, significantly more than the low-metallicity component which dominates the total H I absorption. Consider the case of this same system observed at a lower resolution, or of a composite spectrum which averages the absorption of many such systems (e.g. Steidel et al. 2010). In this case, the metal absorption for individual components can no longer be matched to their respective H I, and we must measure the metallicity for the system as a whole. We showed in §2.5 that doing this results in a low metallicity, $[\text{O}/\text{H}] \approx -1.9$. Thus the high metallicity partial LLSs would escape detection. An even more interesting case to consider is if the low-metallicity component had been more highly ionized, which would occur if it was illuminated by a stronger radiation field, or if it had a lower total N_{H} , reducing its ability to self-shield. To explore this case we ran photoionization models for a range of U values, using $N_{\text{H}0} = 10^{17} \text{ cm}^{-2}$, and with other properties identical to the D component. These show that for a total $N_{\text{H}} \leq 10^{20} \text{ cm}^{-2}$, characteristic of cold streams (Fumagalli et al. 2011), the strongest low-ion metal transition lying outside the Ly α forest⁹, C II $\lambda 1334$, always has a column density $< 10^{13.1} \text{ cm}^{-2}$. Such a weak line approaches the detection limit even for echelle spectra. In low-resolution or composite spectra it would be easily swamped by stronger absorption from any kinematically nearby, metal-enriched gas, and the total metallicity inferred for the system would be dominated by metal-rich components. Therefore a large reservoir of metal-poor gas may be missed by existing studies of the $z \sim 2.5$ CGM that use only low-resolution or composite spectra. Further studies employing high-resolution spectra of background QSOs near foreground galaxies are essential to accurately assess the metal content of the CGM.

By creating a large sample of similar absorption systems where metallicity measurements can be made at small impact parameters, we can realise the exciting possibility of mapping the enrichment distribution of the high-redshift CGM. Both our group and others (e.g. Rudie et al. 2012) are pursuing programs to assemble such a sample.

We thank J.O’Meara for a preliminary reduction of J1444535+291905, and the referee, whose comments improved the paper.

REFERENCES

⁸ We estimate the chance of a random sub-DLA falling within 250 km s^{-1} of the galaxy redshift at $< 2.2\%$ based on the 12 QSO-galaxy pairs searched to find this system.

⁹ Higher ionization states Si IV and C IV cannot be used to detect this gas as they also arise in another co-spatial gas phase.

- Bielby, R., Hill, M. D., Shanks, T., Crighton, N. H. M., Infante, L., Bornancini, C. G., Francke, H., Héraudeau, P., Lambas, D. G., Metcalfe, N., Minniti, D., Padilla, N., Theuns, T., Tummangpak, P., & Weilbacher, P. 2013, *MNRAS*, 430, 425
- Birnboim, Y., & Dekel, A. 2003, *MNRAS*, 345, 349
- Bouché, N., Murphy, M. T., Kacprzak, G. G., Péroux, C., Contini, T., Martin, C., & Dessauges-Zavadsky, M. 2013, *ArXiv e-prints*
- Bryan, G. L., & Norman, M. L. 1998, *ApJ*, 495, 80
- Chen, H.-W., Kennicutt, Jr., R. C., & Rauch, M. 2005, *ApJ*, 620, 703
- Churchill, C. W., Kacprzak, G. G., Steidel, C. C., Spitler, L. R., Holtzman, J., Nielsen, N. M., & Trujillo-Gomez, S. 2012, *ApJ*, 760, 68
- Davé, R., Finlator, K., & Oppenheimer, B. D. 2012, *MNRAS*, 421, 98
- Erb, D. K., Shapley, A. E., Pettini, M., Steidel, C. C., Reddy, N. A., & Adelberger, K. L. 2006a, *ApJ*, 644, 813
- Erb, D. K., Steidel, C. C., Shapley, A. E., Pettini, M., Reddy, N. A., & Adelberger, K. L. 2006b, *ApJ*, 647, 128
- Faucher-Giguère, C.-A., & Kereš, D. 2011, *MNRAS*, 412, L118
- Ferland, G. J., Korista, K. T., Verner, D. A., Ferguson, J. W., Kingdon, J. B., & Verner, E. M. 1998, *PASP*, 110, 761
- Field, G. B., & Steigman, G. 1971, *ApJ*, 166, 59
- Fox, A. J., Petitjean, P., Ledoux, C., & Srianand, R. 2007, *ApJ*, 668, L15
- Fumagalli, M., Prochaska, J. X., Kasen, D., Dekel, A., Ceverino, D., & Primack, J. R. 2011, *MNRAS*, 418, 1796
- Goardt, T., Dekel, A., Sternberg, A., Gnat, O., & Ceverino, D. 2012, *MNRAS*, 424, 2292
- Haardt, F., & Madau, P. 2012, *ApJ*, 746, 125
- Jenkins, E. B. 2009, *ApJ*, 700, 1299
- Kacprzak, G. G., Churchill, C. W., Steidel, C. C., Spitler, L. R., & Holtzman, J. A. 2012, *MNRAS*, 427, 3029
- Keisler, R., Reichardt, C. L., Aird, K. A., Benson, B. A., Bleem, L. E., Carlstrom, J. E., Chang, C. L., Cho, H. M., Crawford, T. M., Crites, A. T., de Haan, T., Dobbs, M. A., Dudley, J., George, E. M., Halverson, N. W., Holder, G. P., Holzzapfel, W. L., Hoover, S., Hou, Z., Hrubes, J. D., Joy, M., Knox, L., Lee, A. T., Leitch, E. M., Lueker, M., Luong-Van, D., McMahon, J. J., Mehl, J., Meyer, S. S., Millea, M., Mohr, J. J., Montroy, T. E., Natoli, T., Padin, S., Plagge, T., Pryke, C., Ruhl, J. E., Schaffer, K. K., Shaw, L., Shirokoff, E., Spieler, H. G., Staniszewski, Z., Stark, A. A., Story, K., van Engelen, A., Vanderlinde, K., Vieira, J. D., Williamson, R., & Zahn, O. 2011, *ApJ*, 743, 28
- Kereš, D., Katz, N., Weinberg, D. H., & Davé, R. 2005, *MNRAS*, 363, 2
- Kimm, T., Slyz, A., Devriendt, J., & Pichon, C. 2011, *MNRAS*, 413, L51
- Krogager, J.-K., Fynbo, J. P. U., Møller, P., Ledoux, C., Noterdaeme, P., Christensen, L., Milvang-Jensen, B. & Sparre, M., 2012, *MNRAS*, 424, L1
- Lehner, N., Howk, J. C., Tripp, T. M., Tumlinson, J., Prochaska, J. X., O'Meara, J. M., Thom, C., Werk, J. K., Fox, A. J., & Ribaud, J. 2013, *ApJ*, 770, 138
- Nelson, D., Vogelsberger, M., Genel, S., Sijacki, D., Kereš, D., Springel, V., & Hernquist, L. 2013, *MNRAS*, 429, 3353
- Oppenheimer, B. D., Davé, R., Kereš, D., Fardal, M., Katz, N., Kollmeier, J. A., & Weinberg, D. H. 2010, *MNRAS*, 406, 2325
- Pettini, M., & Cooke, R. 2012, *MNRAS*, 425, 2477
- Pettini, M., Rix, S. A., Steidel, C. C., Adelberger, K. L., Hunt, M. P., & Shapley, A. E. 2002, *ApJ*, 569, 742
- Pettini, M., Shapley, A. E., Steidel, C. C., Cuby, J.-G., Dickinson, M., Moorwood, A. F. M., Adelberger, K. L., & Gialisco, M. 2001, *ApJ*, 554, 981
- Prochaska, J. X., Henry, R. B. C., O'Meara, J. M., Tytler, D., Wolfe, A. M., Kirkman, D., Lubin, D., & Suzuki, N. 2002, *PASP*, 114, 933
- Prochter, G. E., Prochaska, J. X., O'Meara, J. M., Burles, S., & Bernstein, R. A. 2010, *ApJ*, 708, 1221
- Rakic, O., Schaye, J., Steidel, C. C., & Rudie, G. C. 2011, *MNRAS*, 414, 3265
- Ribaud, J., Lehner, N., Howk, J. C., Werk, J. K., Tripp, T. M., Prochaska, J. X., Meiring, J. D., & Tumlinson, J. 2011, *ApJ*, 743, 207
- Rolleston, W. R. J., Venn, K., Tolstoy, E., & Dufton, P. L. 2003, *A&A*, 400, 21
- Rudie, G. C., Steidel, C. C., Trainor, R. F., Rakic, O., Bogosavljević, M., Pettini, M., Reddy, N., Shapley, A. E., Erb, D. K., & Law, D. R. 2012, *ApJ*, 750, 67
- Rudie, G. C. 2013, PhD thesis, CaltechTHESIS:05202013-155707736
- Savage, B. D., & Sembach, K. R. 1991, *ApJ*, 379, 245
- Schaye, J., Aguirre, A., Kim, T.-S., Theuns, T., Rauch, M., & Sargent, W. L. W. 2003, *ApJ*, 596, 768
- Shen, S., Madau, P., Guedes, J., Mayer, L., Prochaska, J. X., & Wadsley, J. 2013, *ApJ*, 765, 89
- Simcoe, R. A., Sargent, W. L. W., & Rauch, M. 2002, *ApJ*, 578, 737
- Simcoe, R. A., Sargent, W. L. W., & Rauch, M. 2004, *ApJ*, 606, 92
- Simcoe, R. A., Sargent, W. L. W., Rauch, M., & Becker, G. 2006, *ApJ*, 637, 648
- Steidel, C. C. 1990, *ApJS*, 74, 37
- Steidel, C. C., Erb, D. K., Shapley, A. E., Pettini, M., Reddy, N., Bogosavljević, M., Rudie, G. C., & Rakic, O. 2010, *ApJ*, 717, 289
- Stewart, K. R., Kaufmann, T., Bullock, J. S., Barton, E. J., Maller, A. H., Diemand, J., & Wadsley, J. 2011, *ApJ*, 738, 39
- Stinson, G. S., Brook, C., Macciò, A. V., Wadsley, J., Quinn, T. R., & Couchman, H. M. P. 2013, *MNRAS*, 428, 129
- Tripp, T. M., Jenkins, E. B., Bowen, D. V., Prochaska, J. X., Aracil, B., & Ganguly, R. 2005, *ApJ*, 619, 714
- van de Voort, F., Schaye, J., Altay, G., & Theuns, T. 2012, *MNRAS*, 421, 2809
- Webb, J. K., Carswell, R. F., Irwin, M. J., & Penston, M. V. 1991, *MNRAS*, 250, 657

Table 1
Absorption parameters

Ion	z	b (km s ⁻¹)	$\log_{10} N$ (VPFIT) (cm ⁻²)	$\log_{10} N$ (AOD) (cm ⁻²)	Adopted $\log_{10} N$ (cm ⁻²)	AOD Transition (λ_{rest} , Å)
D component (one component at -218 km s ⁻¹ , AOD range -248.5 to -193.5 km s ⁻¹)						
H I	2.436599(01)	< 18	19.50 ± 0.16	–	19.50 ± 0.16	
D I		10.60 ± 0.53	14.93 ± 0.02	$14.976^{+0.061}_{-0.064}$	14.93 ± 0.06	937
Al II		10.42 ^a	11.96 ± 0.02	$11.980^{+0.071}_{-0.075}$	$11.980^{+0.071}_{-0.075}$	1670
C II		11.4 ± 0.2	14.04 ± 0.01	$14.014^{+0.018}_{-0.018}$	$14.014^{+0.018}_{-0.018}$	1334
C II*			< 13.1	$13.863^{+0.018}_{-0.018}$	< 13.1	1335.7
C IV			< 12.15	$12.115^{+0.377}_{-0.862}$	< 12.15	1548
Fe II		7.40 ^a	12.98 ± 0.04	$13.015^{+0.088}_{-0.082}$	$13.015^{+0.088}_{-0.082}$	2600
Mg I			–	< 13.9	< 13.9	1683
Mg II		13.7 ± 0.8	13.20 ± 0.02	$13.198^{+0.102}_{-0.094}$	$13.198^{+0.102}_{-0.094}$	2803
N II			< 13.3	< 13.901	< 13.3	1084
N V			< 12.3	< 12.558	< 12.3	1242
O I	2.436590(01) ^b	8.6 ± 0.13	14.303 ± 0.005	$14.261^{+0.014}_{-0.013}$	$14.261^{+0.047}_{-0.013}$	1302
O VI			< 13.1	< 13.323	< 13.1	1031
Si II		10.43 ± 0.17^a	13.36 ± 0.006	$13.329^{+0.049}_{-0.051}$	$13.329^{+0.049}_{-0.051}$	1526
Si IV			< 12.30	$12.323^{+0.118}_{-0.146}$	< 12.30	1393
Partial LLS 1 (one component at -21 km s ⁻¹ , AOD range -38 to -6 km s ⁻¹)						
H I	2.438862(04)	14.4 ± 1.7	16.30 ± 0.20	–	16.30 ± 0.20	
Al II		4.91 ^a	11.63 ± 0.03	$11.642^{+0.087}_{-0.107}$	$11.642^{+0.087}_{-0.107}$	1670
C II		7.35 ^a	13.66 ± 0.02	$13.674^{+0.015}_{-0.015}$	$13.674^{+0.015}_{-0.015}$	1334
C II*			< 11.9	< 12.021	< 11.9	1335.7
C IV			> 14.3 ^c	> 14.29 ^c	> 14.3	1550
Fe II			< 12.08	$12.067^{+0.335}_{-0.712}$	$12.067^{+0.335}_{-0.712}$	2600
Mg I			–	< 13.8	< 13.8	1683
Mg II		5.17 ^a	12.61 ± 0.04	$12.681^{+0.084}_{-0.087}$	$12.681^{+0.084}_{-0.087}$	2796
N II			< 13.56	< 13.787	< 13.56	1084
N V			< 13.5	< 13.541	< 13.5	1238
O I			< 12.18	< 12.349	< 12.18	1302
O VI			< 14.5	$14.290^{+0.019}_{-0.018}$	< 14.5	1037
Si II		4.81 ± 0.27^a	12.83 ± 0.01	$12.811^{+0.096}_{-0.101}$	$12.811^{+0.096}_{-0.101}$	1526
Si IV			< 13.82	$13.480^{+0.019}_{-0.019}$	< 13.82	1402
Partial LLS 2 (three components at 18, 28, 41 km s ⁻¹ , AOD range 8 to 57.5 km s ⁻¹)						
H I			16.43 ± 0.30	–	16.43 ± 0.30	
Al II			$11.859^{+0.032}_{-0.034}$	$11.851^{+0.087}_{-0.104}$	$11.851^{+0.087}_{-0.104}$	1670
C II			$13.880^{+0.025}_{-0.026}$	$13.856^{+0.015}_{-0.015}$	$13.856^{+0.015}_{-0.015}$	1334
C II*			< 12.1	< 12.114	< 12.1	1335.7
C IV			> 14.4 ^c	> 14.4 ^c	> 14.4	1550
Fe II			< 12.01	< 12.307	< 12.01	2600
Mg I			–	< 13.9	< 13.9	1683
Mg II			$12.865^{+0.041}_{-0.046}$	$12.823^{+0.076}_{-0.076}$	$12.823^{+0.076}_{-0.076}$	2796
N II			< 13.4	$13.316^{+0.072}_{-0.089}$	< 13.4	1084
N V			< 13.45	$13.358^{+0.037}_{-0.041}$	< 13.45	1238
O I			$12.395^{+0.184}_{-0.327}$	$12.439^{+0.383}_{-0.698}$	$12.439^{+0.383}_{-0.698}$	1302
O VI			< 14.5	$14.311^{+0.020}_{-0.020}$	< 14.5	1037
Si II			$13.080^{+0.016}_{-0.017}$	$12.968^{+0.098}_{-0.114}$	$12.968^{+0.098}_{-0.114}$	1526
Si IV			< 13.9	$13.609^{+0.019}_{-0.019}$	< 13.9	1402

Note. — Errors on the AOD column densities include uncertainties in the continuum and zero levels. High-ion upper limits are calculated by measuring the highest column density Voigt profile consistent with the data, assuming thermal broadening.

^a b value is tied to other species assuming purely thermal broadening.

^bA single-component Voigt profile fit to the O I line is offset ~ 0.8 km s⁻¹ from the C II line. This may indicate unresolved component structure, but we do not expect it to significantly affect $N_{\text{O I}}$.

^cSaturated components.